The Astrophysical Journal, 704:196–210, 2009 October 10 doi:10.1088/0004-637X/704/1/196
© 2009. The American Astronomical Society. All rights reserved. Printed in the U.S.A.

LOW MACH NUMBER MODELING OF TYPE IA SUPERNOVAE. IV. WHITE DWARF CONVECTION

M. Zingale[1], A. S. Almgren[2], J. B. Bell[2], A. Nonaka[2], and S. E. Woosley[3]
[1] Department of Physics & Astronomy, Stony Brook University, Stony Brook, NY 11794-3800, USA
[2] Center for Computational Sciences and Engineering, Lawrence Berkeley National Laboratory, Berkeley, CA 94720, USA
[3] Department of Astronomy & Astrophysics, The University of California, Santa Cruz, Santa Cruz, CA 95064, USA
Received 2009 May 22; accepted 2009 August 24; published 2009 September 21

ABSTRACT

We present the first three-dimensional, full-star simulations of convection in a white dwarf preceding a Type Ia supernova, specifically the last few hours before ignition. For these long-time calculations, we use our low Mach number hydrodynamics code, MAESTRO, which we have further developed to treat spherical stars centered in a three-dimensional Cartesian geometry. The main change required is a procedure to map the one-dimensional radial base state to and from the Cartesian grid. Our models recover the dipole structure of the flow seen in previous calculations, but our long-time integration shows that the orientation of the dipole changes with time. Furthermore, we show the development of gravity waves in the outer, stable portion of the star. Finally, we evolve several calculations to the point of ignition and discuss the range of ignition radii.

Key words: convection – hydrodynamics – methods: numerical – nuclear reactions, nucleosynthesis, abundances – supernovae: general – white dwarfs

1. INTRODUCTION

Modeling highly subsonic convection in stars requires algorithms designed for long time integration. In the low Mach number approximation, we filter out sound waves while keeping the compressibility effects important to describing the flow. In our previous work (see Almgren et al. 2006a, henceforth Paper I, Almgren et al. 2006b, henceforth Paper II, and Almgren et al. 2008, henceforth Paper III), we developed a low Mach number stellar hydrodynamics algorithm for reacting full-star flows in order to study the convective phase of Type Ia supernovae (SNe Ia). In Paper I, we derived the low Mach number equation set. In Paper II, we included the effects of heat release due to external sources and allowed for a time-dependent background state. In Paper III, we incorporated reactions into the system and also allowed the background state to evolve in response to large-scale convection and large-scale heating. Here, we extend the algorithm to spherical full-star problems using a three-dimensional Cartesian grid geometry.

Our target application for this algorithm is the period of convection that precedes the ignition of SNe Ia. The standard model of a SN Ia involves a white dwarf in a binary system accreting from a normal companion, and approaching the Chandrasekhar mass (see for example Hillebrandt & Niemeyer 2000). The increase in the central temperature and density accompanying the accretion seed carbon burning in the core, which in turn drives convection in the star. This convective "simmering" phase can last centuries, slowly increasing the core temperature of the white dwarf (Woosley et al. 2004; Wunsch & Woosley 2004). A similar starting condition might be achieved in merging white dwarfs if mass is added slowly enough to avoid ignition at the edge of the stars (Yoon et al. 2007). During this phase, fluid heated by reactions buoyantly rises and cools via expansion, exchanging heat with its surroundings. The extent of the convective region grows with increasing temperature, eventually covering roughly the inner solar mass of the star. Outside of the convective region, the star is stably stratified.

The continued increase in central temperature, coupled with the extreme temperature sensitivity of the carbon reactions, means that eventually the reactions proceed vigorously enough that a hot bubble cannot cool fast enough, and a burning front is born. This happens for a temperature of about (7–8) $\times$ 10^8 K (Nomoto et al. 1984; Woosley 1990). This burning front will quickly propagate through the white dwarf, converting most of the carbon/oxygen fuel to heavier elements, and releasing enough energy to unbind the star. However, exactly where in the star the ignition takes place is still unknown. Among the earliest work to consider the role of buoyancy in off-center ignition were Garcia-Senz & Woosley (1995), Bychkov & Liberman (1995), and Niemeyer et al. (1996). Additionally, some multidimensional studies of the dynamics of the first bubbles to ignite in a white dwarf have been done (Iapichino et al. 2006; Zingale & Dursi 2007). These papers made the case that we really need to understand whether the ignition is at the center or off-center. As calculations have become more sophisticated, it has only become more clear that the outcome of the explosion is extremely sensitive to exactly how the burning fronts are initiated (Gamezo et al. 2005; Jordan et al. 2008; Röpke et al. 2007; García-Senz & Bravo 2005).

Less work has been done on multidimensional modeling of the convective phase preceding the explosion. To date, no multidimensional calculation of the convection in the white dwarf has modeled the entire star. The major contributions thus far are two-dimensional simulations of a 90° wedge of the star using an implicit hydrodynamics code (Höflich & Stein 2002; Stein & Wheeler 2006), and a three-dimensional anelastic calculation (Kuhlen et al. 2006) of the inner convective region of the star. All of these calculations cut out a small part of the central region of the star to avoid the coordinate singularity at the origin in spherical coordinates. Furthermore, the Kuhlen et al. calculation modeled the star out to a radius of only 500 km, leaving out part of the convective zone and the surrounding, stably stratified region. The calculations by Höflich & Stein (2002) found ignition near the center of the white dwarf, produced by the fluid flow converging toward the center, with convective velocities of about 100 km s^{-1}. However, the ignition they see was likely affected by the converging geometry of their computational domain. The three-dimensional calculations by Kuhlen et al. (2006) showed that the large-scale

flow took on a dipole pattern, suggesting that off-center ignition in an *outflow* on one side of the star might be favored. They also investigated the role of rotation. Finally, recent calculations shown in Woosley et al. (2007) used an anelastic method on a Cartesian grid, avoiding the singularity in the center, but still cut out the outer part of the convective region and the convectively stable region surrounding it. Here the dipole was once again seen.

As seen from the wide range of explosion outcomes in the literature, realistic initial conditions are a critical part of SNe Ia modeling. Only simulations of this convective phase can yield the number, size, and distribution of the initial hot spots that seed the flame. Additionally, the initial turbulent velocities in the star are at least as large as the laminar flame speed (Höflich & Stein 2002), so accurately representing this initial flow may be an important component to explosion models. Perhaps owing to a limited number of convection calculations, with few exceptions (Livne et al. 2005), nearly all explosion models to date begin with a quiet (zero velocity) white dwarf.

Our goal in this study is to demonstrate that we have developed low Mach number hydrodynamics to the point where we can perform detailed calculations of the convective flow preceding the explosion, and to begin to understand the nature of the dynamics. In this work, we model the entire star, including the region surrounding the convective zone. Recently, it has been suggested (Piro & Chang 2008) that the dynamics at the interface between the convective and stably stratified regions of the star may be important during the flame propagation phase. Only full star calculations can capture this part of the flow. The resulting simulations can then form the basis for simulations of the flame propagation to build a more detailed picture of SNe Ia.

2. NUMERICAL METHODOLOGY AND SETUP

The basic idea of low Mach number hydrodynamics is to reformulate the fluid equations to filter out sound waves while retaining the compressibility effects important to the problem—in this case, local compressibility effects due to burning, and large-scale effects due to the background stratification of the star. A full derivation of the equations of low Mach number hydrodynamics is presented in Papers I–III. Here we show the final equations and discuss adjustments needed for the spherical star. We recall that the use of low Mach number equations rather than the fully compressible equations enables the use of a time step based on the fluid velocity rather than the sound speed; this allows a $1/M$ increase in the time step over traditional compressible codes, where the Mach number, M, represents the ratio of fluid velocity to sound speed. During the convective phase preceding the first flames in SNe Ia, we expect the Mach number to be $O(0.01)$, making a low Mach number algorithm an appropriate choice.

We choose to discretize our three-dimensional grid using Cartesian rather than spherical coordinates in order to avoid a coordinate singularity at the center of the star. This gives rise to the most notable difference from Paper III—the base state is a one-dimensional radial profile and is not aligned with any of the axes in the three-dimensional Cartesian grid. We refer to this as a spherical geometry, reflecting the fact that the base state is discretized in one-dimensional spherical coordinates. Throughout this paper, we refer to the Cartesian coordinates of the center of the star as (x_c, y_c, z_c).

2.1. Equation Set

The formulation of our equations relies on the existence of a base state density, $\rho_0(r)$, and pressure, $p_0(r)$, that are in hydrostatic equilibrium, $\nabla p_0 = \rho_0 g \mathbf{e}_r$, where $\mathbf{e}_r$ is a unit vector pointing in the radial direction from the center of the star. In spherical geometries, the gravitation acceleration, $g(r)$, is computed solely using the base state density as

$$g(r) = -\frac{GM_{\rm encl}(r)}{r^2}, \tag{1}$$

with the mass enclosed within a radius r defined as

$$M_{\rm encl}(r) = 4\pi \int_0^r \rho_0(r') r'^2 dr'. \tag{2}$$

As we discuss in Section 2.4, we use a cutoff density, $\rho_{\rm cutoff}$, in our initial model. The star is mapped onto the grid down to this cutoff density, surrounded by an ambient medium. In computing $M_{\rm encl}$, we stop contributing to $M_{\rm encl}$ once the density drops below $\rho_{\rm cutoff}$.

In this paper, we reuse much of the notation from Paper III. The overbar represents the average of a quantity over a layer of constant radius in the star

$$\overline{\phi}(r) = \frac{1}{\mathrm{A}(\Omega_H)} \int_{\Omega_H} \phi(\mathbf{x})\, dA, \tag{3}$$

where Ω_H is a region at constant radius in the star, and $\mathrm{A}(\Omega_H) \equiv \int_{\Omega_H} dA$. In this notation, $\mathbf{x}$ represents the Cartesian coordinates on the three-dimensional grid, and r is the base state radial coordinate centered at (x_c, y_c, z_c). A subscript "0" represents a base state quantity. We compute $\mathbf{e}_r$ in a cell indexed by (i, j, k) with Cartesian coordinates (x_i, y_j, z_k) as

$$\mathbf{e}_r = \frac{x_i - x_c}{r}\mathbf{e}_x + \frac{y_j - y_c}{r}\mathbf{e}_y + \frac{z_k - z_c}{r}\mathbf{e}_z, \tag{4}$$

with $r^2 = (x_i - x_c)^2 + (y_j - y_c)^2 + (z_k - z_c)^2$, and $\mathbf{e}_x$, $\mathbf{e}_y$, and $\mathbf{e}_z$ being the unit vectors for the Cartesian coordinate system.

In our previous work, the total fluid velocity, $\mathbf{U}$, was decomposed into a local velocity field, $\widetilde{\mathbf{U}}$, and base state velocity, w_0, as

$$\mathbf{U} = \widetilde{\mathbf{U}}(\mathbf{x}, t) + w_0(r, t)\mathbf{e}_r. \tag{5}$$

The base state velocity is used to adjust the base state in response to the heating on the grid. In Paper II, we demonstrated that when the heating is large, expanding the base state is critical to accurately modeling the flow.

In the current application, convection in the white dwarf, the heating is small until the flame ignites. Therefore, for these first calculations, we use a background state that is fixed in time. We will later quantify the extent to which this assumption of a fixed background state is valid. This simplifies the evolution equations, and we can now use $\mathbf{U}$ for $\widetilde{\mathbf{U}}$ and $w_0 = 0$.

The full state evolves according to

$$\frac{\partial(\rho X_k)}{\partial t} = -\nabla\cdot(\mathbf{U}\rho X_k) + \rho\dot{\omega}_k, \tag{6}$$

$$\frac{\partial \mathbf{U}}{\partial t} = -\mathbf{U}\cdot\nabla\mathbf{U} - \frac{1}{\rho}\nabla\pi - \frac{(\rho - \rho_0)}{\rho} g\mathbf{e}_r. \tag{7}$$

Equation (6) is the species evolution equation, where X_k is the mass fraction of species k, with the creation rate $\dot{\omega}_k$ provided by the nuclear reaction network. The mass density,

ρ, is simply $\rho = \sum_k (\rho X_k)$. For the velocity evolution equation (Equation (7)), π is the dynamic pressure resulting from the asymptotic expansion of the pressure in terms of the Mach number. In Paper III, we also evolved the enthalpy for the sole purpose of getting the temperature to feed into the reaction network. For this paper, we instead define the temperature from ρ, p_0, and X_k. Our experience has shown that, with the spherical geometry, the discretization errors are minimized by using the hydrostatic, radial base state pressure to define temperature. We will revisit this in a future paper. This system of equations is identical to that presented in Paper III, with $\mathbf{U} = \widetilde{\mathbf{U}}$, $w_0 = 0$, and $\partial p_0/\partial t = 0$.

The velocity field is subject to a constraint equation

$$\nabla\cdot(\beta_0\mathbf{U}) = \beta_0 S, \tag{8}$$

with

$$\beta_0(r) = \rho_0(0)\exp\left(\int_0^r \frac{1}{\overline{\Gamma}_1 p_0}\frac{\partial p_0}{\partial r'}\,dr'\right), \tag{9}$$

where $\overline{\Gamma}_1$ is the average over a layer of $d(\log p)/d(\log \rho)$ at constant entropy, and

$$S = -\sigma\sum_k \xi_k\dot{\omega}_k + \frac{1}{\rho p_\rho}\sum_k p_{X_k}\dot{\omega}_k + \sigma H_{\rm nuc}. \tag{10}$$

Here, $p_{X_k} \equiv \partial p/\partial X_k|_{\rho,T,X_{j,j\neq k}}$, $\xi_k \equiv \partial h/\partial X_k|_{p,T,X_{j,j\neq k}}$, $p_\rho = \partial p/\partial\rho|_{T,X_k}$, and $\sigma = p_T/(\rho c_p p_\rho)$, with $p_T \equiv \partial p/\partial T|_{\rho,X_k}$ and $c_p \equiv \partial h/\partial T|_{p,X_k}$ being the specific heat at constant pressure. In these derivatives, h is the specific enthalpy, defined in terms of the specific internal energy, e, pressure, and density as $h = e + p/\rho$. Finally, $H_{\rm nuc}$ is the nuclear energy release (with units of erg g^{-1} s^{-1}) as computed from our reaction network. Physically, S represents the local compressibility effects due to heat release from reactions and composition changes. The presence of the density-like quantity β_0 inside the divergence in the constraint captures the expansion of a parcel of fluid as it rises in the hydrostatically stratified star.

We refer the reader to the extensive comparisons with compressible algorithms in Papers I through III that demonstrate the validity of the low Mach number approximation. For the most part, the algorithm to evolve the star follows closely that described in Paper III. For the construction of the advective terms, the interface states are again constructed using a piecewise linear unsplit Godunov scheme based on that of Colella (1990), but we now use the full corner-coupling scheme developed by Saltzman (1994). In the subsections below, we point out the differences for the present application.

2.2. Mapping

Since the one-dimensional radial base state is not aligned with any of the axes in the three-dimensional Cartesian grid, the discretization of quantities that involve both the base state and the full state becomes complicated. Various parts of the algorithm (such as the averaging operations) require a mapping between the base state and the full state. Because the base state is not aligned with the Cartesian coordinate axes, we are free to choose the base state resolution independent of the Cartesian grid spacing. Numerical experimentation has shown that setting the base state resolution, Δr, to be finer than the Cartesian grid resolution, Δx, gives the best results. (Here we assume $\Delta x = \Delta y = \Delta z$.) For the present simulations, we use $5\Delta r = \Delta x$. We refer to the procedure that maps data from one dimension to three dimensions as `fill_3d`, and the complementary procedure that maps from three dimensions to one dimension as `average`.

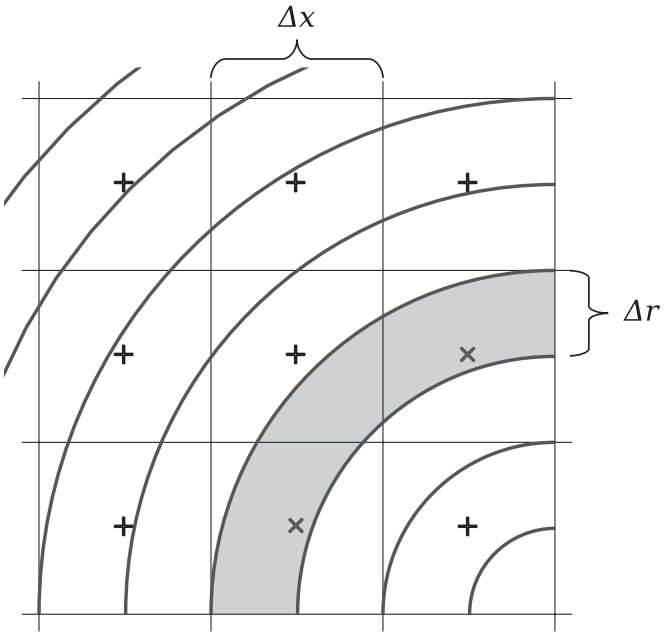

Figure 1. Cartesian grid and spherical base state (shown here in two dimensions for simplicity, using $2\Delta r = \Delta x$). Here we represent the spherical base state as concentric shells (black curved lines). Since the base state is not aligned with the Cartesian grid, we need to map between the two configurations. The "+" symbols represent the Cartesian zone centers. In our mapping from the radial profile to the Cartesian grid, the zones marked with the "×" symbol are assigned the value from the gray-shaded radial bin.

Figure 1 shows the Cartesian grid overlaid by the spherical base state (for simplicity, the figure is drawn in two dimensions using $2\Delta r = \Delta x$). The `fill_3d` procedure computes the distance of the center of cell indexed by (i, j, k) from the center of the star:

$$r = \sqrt{(x_i - x_c)^2 + (y_j - y_c)^2 + (z_k - z_c)^2}. \tag{11}$$

We use this radius to find the corresponding radial bin as $n = \mathtt{int}(r/\Delta r)$ (here, our convention is to use 0-based indexing for the base state). We can then initialize a Cartesian cell quantity q from its corresponding base state quantity, q_0, as $q_{i,j,k} = q_{0,n}$.

For the `average` process, we first define a coarse one-dimensional radial array with $\Delta r_{\rm c} = \Delta x$. Then, for each cell indexed by (i, j, k), we again compute the radius, r, as above, and define the index of the corresponding coarse radial bin, $n_{\rm c} = \mathtt{int}(r/\Delta r_{\rm c})$. We define $q_{0,n_{\rm c}}$ as the average of all the $q_{i,j,k}$ whose Cartesian cell centers map into the coarse radial bin $n_{\rm c}$. Next, we construct edge-centered states on the coarse radial bin using the fourth-order approximation, $q_{0,n_{\rm c}+1/2} = (7/12)(q_{0,n_{\rm c}} + q_{0,n_{\rm c}+1}) - (1/12)(q_{0,n_{\rm c}-1} + q_{0,n_{\rm c}+2})$. Finally, for each coarse radial bin, we construct a quadratic profile using $q_{0,n_{\rm c}-1/2}$, $q_{0,n_{\rm c}}$ and $q_{0,n_{\rm c}+1/2}$. This is based on the interpolating polynomial used by the PPM scheme to find edge states (Colella & Woodward 1984). Specifically, for $n_{\rm c}\Delta r_{\rm c} \leqslant r \leqslant (n_{\rm c}+1)\Delta r_{\rm c}$, the interpolating polynomial is

$$q_0(r) = q_{0,n_{\rm c}-1/2} + \xi(r)\left\{\Delta q_{n_{\rm c}} + q_{6,n_{\rm c}}[1 - \xi(r)]\right\}, \tag{12}$$

with

$$\xi(r) = \frac{r - n_{\rm c}\Delta r_{\rm c}}{\Delta r_{\rm c}}, \tag{13}$$

$$\Delta q_{n_c} = q_{0,n_c+1/2} - q_{0,n_c-1/2}, \quad (14)$$

and

$$q_{6,n_c} = 6\left[q_{0,n_c} - \frac{1}{2}\left(q_{0,n_c+1/2} + q_{0,n_c-1/2}\right)\right]. \quad (15)$$

We note that since we are not evolving the base state in the simulation presented here, the feedback from the full state to the base state through `average` is limited to computing $\overline{\Gamma}_1$, as needed for updating β_0.

2.3. Microphysics

We use the general stellar equation of state described by Timmes & Swesty (2000) and Fryxell et al. (2000), which includes contributions from electrons, ions, and radiation. For these calculations, we include the effects of Coulomb corrections included in the publicly available version of this EOS (Timmes 2008).

Our reaction network is unchanged from Paper III, and is a single-step ^{12}C +^{12} C reaction using screening as described in Graboske et al. (1973), Weaver et al. (1978), Alastuey & Jancovici (1978), and Itoh et al. (1979), resulting in ^{24}Mg ash. We release the energy corresponding to the binding energy difference between the magnesium ash and carbon fuel. Paper III provides full details on how the reaction network is solved. Our only change from the implementation there is that we now update the temperature at the end of the reaction step. Finally, we note that we do not call the reaction network for densities below $\rho_{\rm cutoff}$.

We note that by integrating the reaction rate equation, we are dealing with reactions differently than Kuhlen et al. (2006). There, an analytic approximation to the reaction rate was used and evaluated given a temperature and density. Our method extends more easily to a full reaction network. A second difference is that Kuhlen et al. (2006) burned to a mix of neon and magnesium, leading to a slightly lower energy release. This difference may affect the timescales we see in the calculation, but we do not expect it to introduce qualitative differences.

2.4. Initial Model

We begin with an initial one-dimensional white dwarf model produced with the stellar evolution code, Kepler (Weaver et al. 1978). This model was evolved to the point where the central temperature is 6×10^9 K, and the central density is 2.6×10^9 g cm^{-3}. The composition is about half ^{12}C and half ^{16}O, with a small amount ($< 0.5\%$) of ash in the center of the star. The total mass of the star is 1.382 $M_\odot$.

We follow the procedure outlined in Zingale et al. (2002) to convert the initial model from the one-dimensional Lagrangian mesh used by Kepler to the uniformly zoned Eulerian grid used in our calculation. It is important that the initial model satisfy hydrostatic equilibrium discretely with our equation of state on the base state grid we use for our simulation. In particular, we want to enforce the following discretization of hydrostatic equilibrium:

$$p_{0,i+1} - p_{0,i} = \frac{1}{2}\Delta r(\rho_{0,i} + \rho_{0,i+1})g_{i+1/2}. \quad (16)$$

Hydrostatic equilibrium alone does not specify our initial model; therefore, we must also specify the initial temperature. In the interior of the star, where convection dominates, constant entropy is a good approximation. We use this constraint together with Equation (16) and the equation of state to find the temperature, density, and pressure throughout the inner region of the star. For the composition, we use the profile provided by the Kepler model, but since we are using a reduced network, we group together the ^{20}Ne and ^{24}Mg ash into a single composition variable.

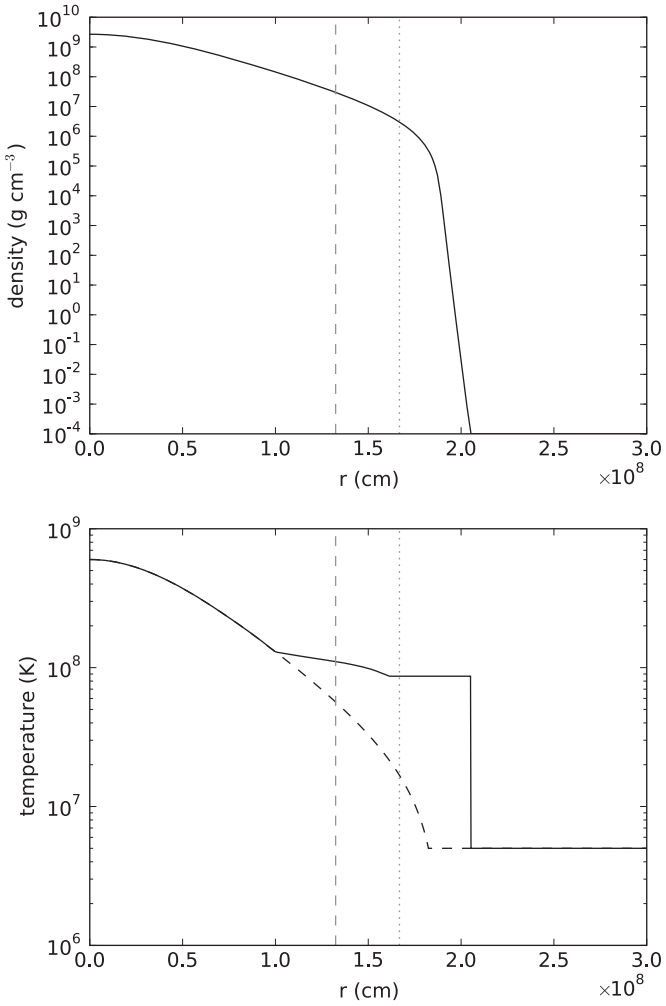

Figure 2. Initial model used for the full star convection calculation. The top panel shows the density, and the bottom panel shows the temperature. In both panels, the vertical dotted gray line represents the location of the low density cutoff—data outside of this cutoff are not used by our calculations. The vertical dashed gray line indicates where our sponge forcing term begins. For the temperature plot, the solid line represents the initial model used in our calculation, and the dashed line represents the temperature structure for a completely isentropic model.

The convective region is surrounded by an outer, convectively stable region. When the isentropic temperature profile drops below the temperature provided by the Kepler model, we switch to using the Kepler temperature. Figure 2 shows our final temperature profile, along with a completely isentropic model for reference. The departure of the two temperature curves marks the boundary of the convective region. The mass of the inner isentropic region of the star is 1.131 $M_\odot$. We note that the spatial extent of the convective zone in the white dwarf is somewhat uncertain. Different assumptions about the accretion history of the white dwarf would lead to different mass convection zones.

Overall, this procedure results in a slight adjustment of the structure of the star compared to the initial Kepler model. The

resulting model serves as the initial base state for our calculation. As discussed in Papers II and III, outside of the star we cannot bring the density down to arbitrarily small values, as that would result in a velocity field that would too severely restrict the time step (a consequence of our constraint equation). In practice, we impose a cutoff at a moderately small density, $\rho_{\rm cutoff}$, and set the density to this constant value outside of the star. For the main calculation presented here, we choose $\rho_{\rm cutoff} = 3 \times 10^6$ g cm^{-3}. While this may sound high, we note that the mass of the star enclosed by $\rho_{\rm cutoff}$ is 1.378 $M_\odot$—a 0.2% difference from the total mass of the star. We note also that as in Paper III, we use an anelastic cutoff, the density below which the coefficient, β_0, of our velocity constraint is defined by keeping β_0/ρ_0 constant. In this paper, we always set the anelastic cutoff to be $\rho_{\rm cutoff}$.

The initial three-dimensional state is set by using the `fill_3d` routine in Section 2.2 to interpolate ρ_0, p_0, $X_{k,0}$, and T_0 to each cell center. The initial velocity field is not as well defined. The one-dimensional stellar evolution code used mixing length theory to describe convective mixing in the interior of the star. When we map the model onto our three-dimensional grid, there is a region that is convectively unstable (corresponding to the region in Figure 2 where $r < 1.0 \times 10^8$ cm). However, there is not enough information in the one-dimensional model to initialize a three-dimensional velocity field that correctly represents the convective field.

If we start with zero initial velocity, then at $t = 0$ the reactions near the core generate a large amount of energy, and the highly nonlinear form of the reaction rate means that the energy release quickly grows. Without an initial velocity field to advect some of this energy away from the core, the energy generation grows too quickly, and an unphysical runaway occurs. However, by starting with an initial nonzero velocity field, our simulation very quickly finds a convective velocity field that balances the energy generation at the core. Thus, we define a set of Fourier modes

$$C^{(x)}_{l,m,n} = \cos\left(\frac{2\pi l x}{\sigma} + \phi^{(x)}_{l,m,n}\right) \tag{17a}$$

$$C^{(y)}_{l,m,n} = \cos\left(\frac{2\pi m y}{\sigma} + \phi^{(y)}_{l,m,n}\right) \tag{17b}$$

$$C^{(z)}_{l,m,n} = \cos\left(\frac{2\pi n z}{\sigma} + \phi^{(z)}_{l,m,n}\right), \tag{17c}$$

and

$$S^{(x)}_{l,m,n} = \sin\left(\frac{2\pi l x}{\sigma} + \phi^{(x)}_{l,m,n}\right) \tag{18a}$$

$$S^{(y)}_{l,m,n} = \sin\left(\frac{2\pi m y}{\sigma} + \phi^{(y)}_{l,m,n}\right) \tag{18b}$$

$$S^{(z)}_{l,m,n} = \sin\left(\frac{2\pi n z}{\sigma} + \phi^{(z)}_{l,m,n}\right), \tag{18c}$$

where σ is the characteristic scale of the perturbation, and the $\phi^{\{x,y,z\}}_{l,m,n}$ are randomly generated phases between $[0, 2\pi]$. We then compute the total contribution to the velocity perturbation from the modes as

$$u' = \sum_{l=1}^{3}\sum_{m=1}^{3}\sum_{n=1}^{3} \frac{1}{N_{l,m,n}}\left[-\gamma_{l,m,n} m C^{(x)}_{l,m,n} C^{(z)}_{l,m,n} S^{(y)}_{l,m,n} + \beta_{l,m,n} n C^{(x)}_{l,m,n} C^{(y)}_{l,m,n} S^{(z)}_{l,m,n}\right] \tag{19a}$$

$$v' = \sum_{l=1}^{3}\sum_{m=1}^{3}\sum_{n=1}^{3} \frac{1}{N_{l,m,n}}\left[\gamma_{l,m,n} l C^{(y)}_{l,m,n} C^{(z)}_{l,m,n} S^{(x)}_{l,m,n} - \alpha_{l,m,n} n C^{(x)}_{l,m,n} C^{(y)}_{l,m,n} S^{(z)}_{l,m,n}\right] \tag{19b}$$

$$w' = \sum_{l=1}^{3}\sum_{m=1}^{3}\sum_{n=1}^{3} \frac{1}{N_{l,m,n}}\left[-\beta_{l,m,n} l C^{(y)}_{l,m,n} C^{(z)}_{l,m,n} S^{(x)}_{l,m,n} + \alpha_{l,m,n} m C^{(x)}_{l,m,n} C^{(z)}_{l,m,n} S^{(y)}_{l,m,n}\right], \tag{19c}$$

where $\alpha_{l,m,n}$, $\beta_{l,m,n}$, and $\gamma_{l,m,n}$ are randomly generated amplitudes between $[-1, 1]$, and $N_{l,m,n} = \sqrt{l^2 + m^2 + n^2}$ is the normalization,

A perturbational velocity field is then computed as

$$u'' = \frac{A u'}{2}\left[1 + \tanh\left(\frac{r_{\rm pert} - r}{d}\right)\right] \tag{20a}$$

$$v'' = \frac{A v'}{2}\left[1 + \tanh\left(\frac{r_{\rm pert} - r}{d}\right)\right] \tag{20b}$$

$$w'' = \frac{A w'}{2}\left[1 + \tanh\left(\frac{r_{\rm pert} - r}{d}\right)\right], \tag{20c}$$

where the tanh profile gradually cuts off the perturbation at a radius $r_{\rm pert}$ with a transition thickness d. Finally, the initial velocity field is computed by applying the projection to $(u,'' v,'' w'')$ to ensure that it satisfies the divergence constraint. We pick the amplitude, A, to be small, and independent of the velocities used in the one-dimensional stellar evolution model. Once the flow field is established, we expect the details of the initial velocity field to be forgotten. This is an area we will explore in a subsequent paper.

Throughout the calculation, we solve the reaction network to compute the energy release that drives the convection. By starting at a low initial central temperature, we thus expect a realistic flow field to build up over time as the central temperature increases from the reactions. In this respect, we differ from the initialization procedure used in Kuhlen et al. (2006). In their anelastic approximation, they carried the perturbational temperature separately from the base state temperature, and to initialize the flow field they evaluated the carbon burning heating term using only the base state temperature. By excluding the perturbational temperature, they left out the nonlinear feedback in the extremely temperature-sensitive carbon reaction rate, and therefore built a flow field without the chance of runaway. Once the flow field was established, they fed the temperature perturbations back into the reaction rate to watch the runaway.

2.5. Sponging

As described in Paper III, we use a sponge to damp the velocities outside of our region of interest. We use the same functional form here, with the velocity forcing given by

$$\mathbf{U}^{\rm new} = \mathbf{U}^{\rm old} - \Delta t\, \kappa f_{\rm damp} \mathbf{U}^{\rm new}, \tag{21}$$

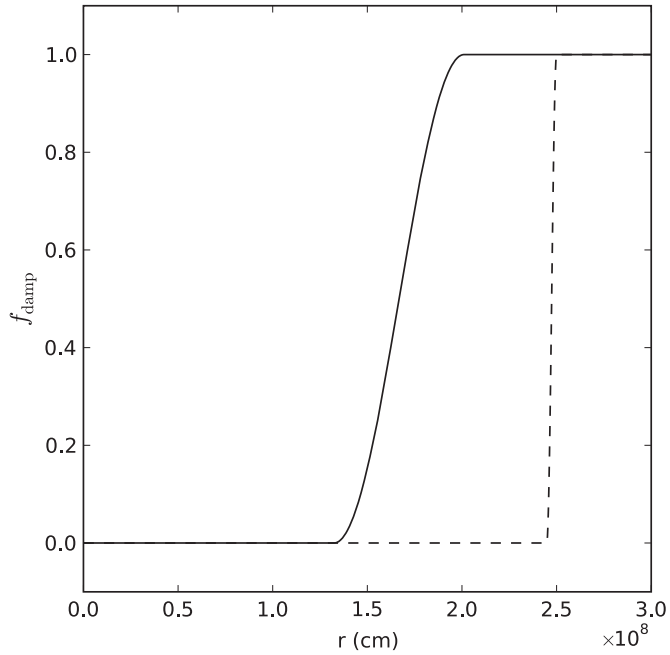

Figure 3. Inner sponge function, $f_{\rm damp}$, as a function of radius for $\rho_{\rm cutoff} = 3 \times 10^6$ g cm^{-3} (solid line), and the outer sponge function for $D = 5 \times 10^8$ cm and a 384^3 grid (dashed).

where κ is a frequency. For all results presented here, we use $\kappa = 10\,{\rm s}^{-1}$. The sponge factor has the form

$$f_{\rm damp} = \begin{cases} 0 & \text{if } r < r_{\rm sp} \\ \frac{1}{2}\left\{1 - \cos\left[\pi\left(\frac{r - r_{\rm sp}}{r_{\rm tp} - r_{\rm sp}}\right)\right]\right\} & \text{if } r_{\rm sp} \leqslant r < r_{\rm tp}. \\ 1 & \text{if } r \geqslant r_{\rm tp}. \end{cases} \quad (22)$$

The quantity $r_{\rm sp}$ represents the radius where the sponging term gradually begins to turn on, and is set to the radius corresponding to $10{\cdot}\rho_{\rm cutoff}$. The top of the sponge, $r_{\rm tp}$, where the sponge is in full effect is set as $r_{\rm tp} = 2r_{\rm md} - r_{\rm sp}$, with $r_{\rm md}$ set to the radius corresponding to the $\rho_{\rm cutoff}$. As noted above, we use a $\rho_{\rm cutoff} = 3 \times 10^6$ g cm^{-3} for these calculations, so the corresponding density where our sponging begins is 3×10^7 g cm^{-3}. Based on our initial model, 1.320 $M_\odot$ of the star is contained within $r_{\rm sp}$—the sponge only affects the very outer portion of the star. Figure 2 shows the location of $r_{\rm sp}$ for our initial model—we see that it is well outside the convectively unstable region. Figure 3 shows $f_{\rm damp}$ versus r for $\rho_{\rm cutoff} = 3 \times 10^6$ g cm^{-3}.

This sponge is effective in damping the velocities at the edge of the star. Our domain is $D = 5 \times 10^8$ cm on a side, so the distance from the center of the star along one of the coordinate axes to the edge of the domain is 2.5×10^8 cm. The distance from the center to a corner of the domain is $\sqrt{3}$ larger. Because we are placing a spherical star in a cubic domain, we found that we need an additional sponge to damp the velocities in the outer corners of the domain—well outside of the star. We define an outer sponge of the same form as above, but with $r_{\rm tp} = D/2$ and $r_{\rm sp} = r_{\rm tp} - 4\Delta x$, where Δx is the grid spacing, and κ set to 10 times the value of the inner sponge. This additional sponge is included in the momentum equation in the same fashion as the inner sponge. Figure 3 shows the profile of this additional sponge as well.

3. RESULTS

Our main goal in these simulations is to study the convection in the white dwarf up to the point of ignition. In this section, we present results for our main 384^3 convection calculation, supporting calculations with lower resolution, as well as a test problem. In each case, the code was run with an advective CFL number of 0.5 with the star centered in a domain 5×10^8 cm on a side.

3.1. Test Problem: Isentropically Stratified Star

To test the interaction between the spherical base state and the three-dimensional Cartesian representation of the star, we perform a simple advection test with an analytic solution. First, we construct a completely isentropic initial model. This is achieved by picking a central density of 2.6×10^9 g cm^{-3} and a central temperature of 6×10^8 K, and a uniform composition of 0.3 ^{12}C and 0.7 ^{16}O, and integrating outward using our hydrostatic equilibrium constraint, Equation (16), and forcing the entropy to be constant through the equation of state. We initialize the full state using the isentropic base state with no perturbations. We also set $\beta_0 = \rho_0$ discretely (which is true analytically for an isentropic base state and constant $\overline{\Gamma}_1$), and disable all reactions and heating. The constraint is now identical to the anelastic constraint, $\nabla \cdot (\rho_0 U) = 0$.

Under these conditions, the continuity equation becomes

$$\frac{\partial \rho}{\partial t} = -\nabla \cdot (\rho U) = -\nabla \cdot (\rho_0 U) = 0, \quad (23)$$

using the fact that $\rho = \rho_0$ initially, and the anelastic constraint. As a result, we see that the density should remain constant in the star regardless of the velocity field.

This provides a means to test our mapping procedure. If we start with an isentropically stratified star and seed a random velocity field, the density should not change with time. For our test, we start with a random velocity field described by Equation (26). For the amplitude of the perturbation, we set $A = 10^7$ cm s^{-1}—this is typical of the highest velocities we expect to see in our convection calculations. For the size of the perturbation, we set $r_{\rm pert} = 5 \times 10^7$ cm—this value represents about half the size of the expected convective region in the white dwarf. Finally, we set the characteristic wavelength of the perturbation, $\sigma = 10^7$ cm. We make the transition between the perturbation and the ambient star sharp, effectively smaller than our grid resolution, setting $d = 10^5$ cm. The resolution is 384^3, the same as that used in the main calculation in the following section.

To assess the change in density with time, we will look at the average density, $\langle \rho \rangle$, as a function of radius, and the deviation of the density as a function of radius, $\delta\rho$. We define these as

$$\langle \rho \rangle_r = \frac{1}{N_{\Omega_r}} \sum_{\Omega_r} \rho, \quad (24)$$

where Ω_r is the set of cells in the computational domain whose center falls within the radial bin at radius r, and N_{Ω_r} is the number of cells in Ω_r. The rms fluctuations are

$$(\delta\rho)_r = \left[\frac{1}{N_{\Omega_r}} \sum_{\Omega_r} (\rho - \rho_0)^2\right]^{1/2}. \quad (25)$$

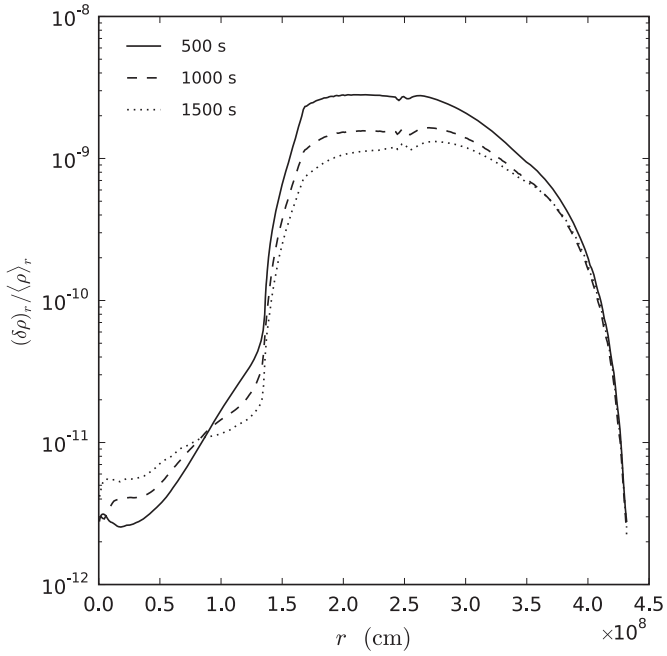

Figure 4. $(\delta\rho)_r/\langle\rho\rangle_r$ vs. r for the test problem at 3 times. We see that the relative change in density resulting from a large amplitude velocity perturbation is small.

Here we recognize that the base state density, ρ_0, represents the average density at a given radius. We compute and store $(\rho - \rho_0)$ for every zone in our computational domain directly in the code as the simulation runs, and then compute $(\delta\rho)_r$ using Equation (33) with a radial bin spacing $\Delta r = \Delta x$—this ensures that no interpolation is needed to fill radial cells.

Figure 4 shows a plot of $(\delta\rho)_r/\langle\rho\rangle_r$ versus r at several times. By normalizing to the average density, $\langle\rho\rangle_r$, we are seeing a measure of the relative error in the density from our advection scheme. As the plot shows, even after 1500 s of evolution, the error at the center of the star is $< 10^{-11}$. Once we are outside of the star $r > 2 \times 10^8$ cm, the error rises, but still stays below 5×10^{-9} everywhere. This demonstrates that our algorithm accurately preserves $\partial\rho/\partial t = 0$ in the limiting case of an isentropic model with no heating and $\beta_0 = \rho_0$.

3.2. Convection in a White Dwarf

We model convection in the white dwarf by mapping the initial model described in Section 2.4 onto our Cartesian grid. For the initial velocity field, we use $A = 10^5$ cm s^{-1}, $d = 10^5$ cm, $r_{\rm pert} = 2 \times 10^7$ cm, and $\sigma = 10^7$ cm.

3.2.1. Diagnostics

To help us understand the character of the flow in our calculations, we make use of several diagnostic quantities. We define the region of interest of the domain, $\Omega_{\rm star}$, to be those computational cells with $\rho > \rho_{\rm cutoff}$, where we have used $\rho_{\rm cutoff} = 3 \times 10^6$ g cm^{-3} unless otherwise specified. The diagnostics defined below are computed every time step, as the code is running.

The peak temperature in the domain is simply

$$T_{\rm peak} = \max_{\Omega_{\rm star}}\{T\}. \tag{26}$$

As the temperature in the star increases considerably toward the center of the star, we expect the peak temperature to be close to (but not exactly equal to) the central temperature.

Motivated by previous results that suggest a dipole nature to the flow (Kuhlen et al. 2006), we look at several diagnostics based on the radial fluid velocity. First, we define the radial velocity to be $v_r = \mathbf{U}\cdot\mathbf{e}_r$. Then we compute components of the density-weighted average radial velocity in each coordinate direction

$$\langle\tilde{v}_r\rangle_x = \sum_{N_{\Omega_{\rm star}}} \rho v_r \left(\frac{x - x_c}{r}\right) \Big/ \sum_{N_{\Omega_{\rm star}}} \rho, \tag{27}$$

where r is the distance of a given zone from the center of the star, and $N_{\Omega_{\rm star}}$ is the number of computational zones contained in the domain $\Omega_{\rm star}$. We compute $\langle\tilde{v}_r\rangle_y$ and $\langle\tilde{v}_r\rangle_z$ analogously, using $(y - y_c)$ and $(z - z_c)$, respectively. The relative magnitudes of the components of $\langle\tilde{v}_r\rangle_i$ tell us about the direction of any dipole nature to the flow. In particular, we can derive the directional angles ϕ in the x–y plane, and θ as measured from the z-axis as

$$\phi = \tan^{-1}\left(\frac{\langle\tilde{v}_r\rangle_y}{\langle\tilde{v}_r\rangle_x}\right) \tag{28}$$

and

$$\theta = \tan^{-1}\left(\frac{\sqrt{\langle\tilde{v}_r\rangle_x^2 + \langle\tilde{v}_r\rangle_y^2}}{\langle\tilde{v}_r\rangle_z}\right). \tag{29}$$

We could have instead computed the average radial velocity without a density weighting, but because we are summing over the entire star (where $\rho > \rho_{\rm cutoff}$), we are including the outer convectively stable region in the average, where we do not expect to see much influence from the dipole. By density weighting, we are giving more weight to the center of the star, where the convective pattern dominates.

Finally, to get a sense of scale for the radial velocity in the star, we compute

$$(v_r)_{\rm peak} = \max_{\Omega_{\rm star}}\{|v_r|\}. \tag{30}$$

3.2.2. Long-term Convective Behavior

Our main result is a 384^3 calculation of convection in a white dwarf, starting from an initial model with a central temperature of 6×10^8 K. Our computational domain is 5×10^8 cm on a side, giving us 13 km zones. Our goal is to follow the convection as reactions bring the central temperature up over 7×10^8 K and into the regime of ignition.

As noted in Section 2.4, we started with a small velocity perturbation near the center of the star and the velocity otherwise zero. As the simulation begins, reactions heat the core of the star, and since the background of the star is isentropic, the heated fluid at the core begins to buoyantly move radially outward. Figure 5 shows the magnitude of the vorticity ($|\nabla \times \mathbf{U}|$) in the three orthogonal slice planes through the center of the star at several different times. At early times, we see convective flow developing near the center of the star. By 400 s, the convective flow has grown to fill the convectively stable region, and we see gravity waves excited in the stable region above. The later times show the convective pattern continuing to strengthen, with small asymmetries in the vorticity moving through the inner convective region. For most of the simulation, we see a sharp distinction in the character of the flow at the boundary of the isentropic region in the star. However, toward the very end of the calculation, as shown in the very last pane of Figure 5, we

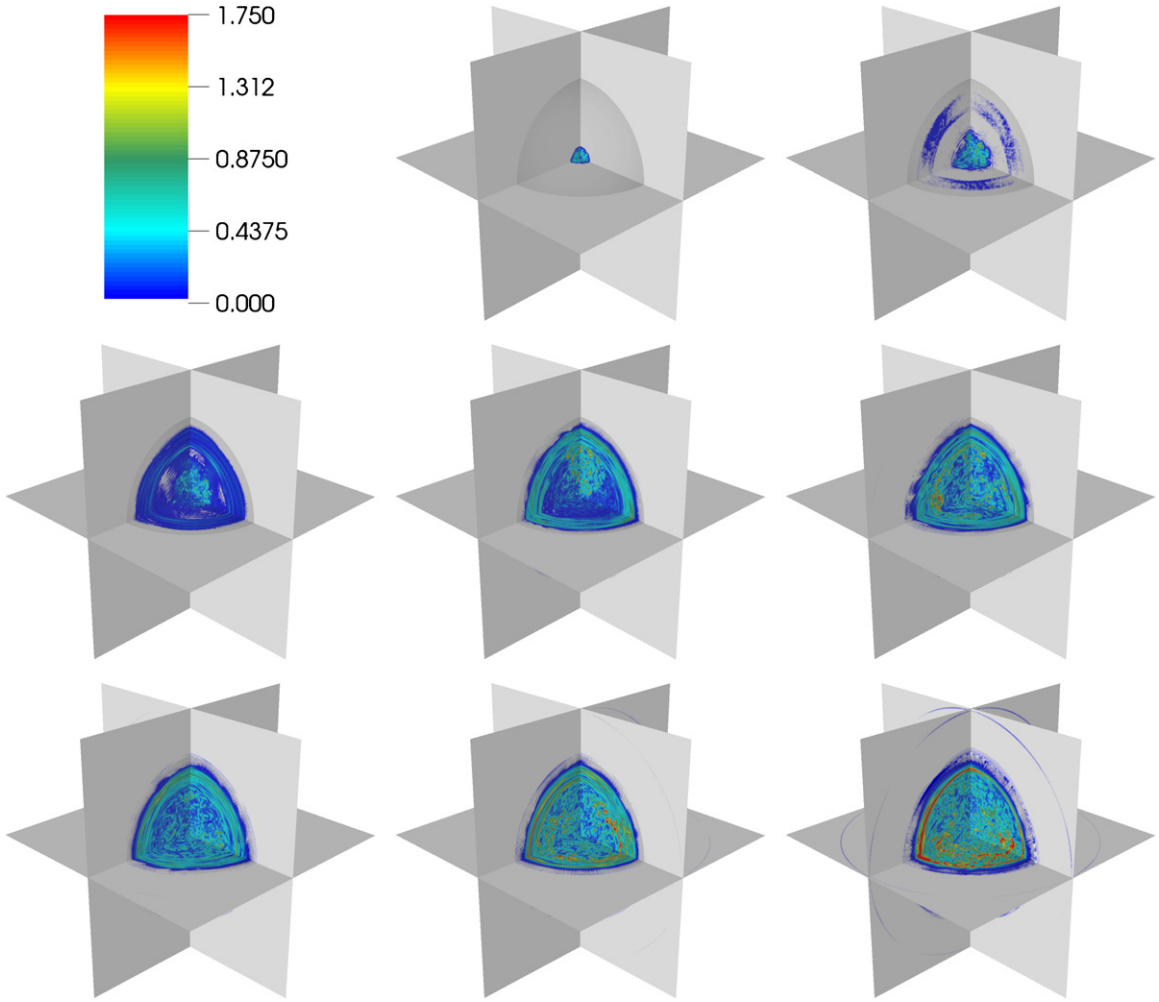

Figure 5. Development of the convective flow in the 384^3 calculation. Here we plot vorticity. The data scale is capped at 1.75 s^{-1}, even though the maximum vorticity steadily climbs as the simulation progresses, reaching over 13 s^{-1} by the last panel. From left to right, top to bottom, the panels show the vorticity at 50, 100, 200, 400, 800, 1600, 3200, and 6400 s.

no longer see the separation between the two regions, and the convective plumes appear to travel through the entire star.

Figure 6 shows contours of the radial velocity at four different times. Qualitatively, these times represent the early period (panel a, 800 s), two intermediate snapshots (panels b and c, 3200 and 3420 s, respectively), and the very late stage of the calculation (panel d, 7132 s). Red color indicates fluid moving radially outward, and blue color indicates fluid moving radially inward. The gray surface is drawn at a constant density ($\rho = \rho_{\rm cutoff}$) and represents the surface of the star. Very early we see the distinct asymmetric nature to the flow characteristic of a dipole flow. The dipole is not nearly as symmetric as that shown in Kuhlen et al. (2006), perhaps due to differing resolution or the inclusion of the stably stratified layer surrounding the convective region in our study. In general, the outward moving fluid appears more coherent then the inward moving fluid. Comparing the images at different times, we see that the dipole direction changes with time. Occasionally, the flow takes on a more organized form, with the inward moving fluid forming a concentric ring around the outward flow, as shown in panel c. At the very late stages of the simulation (panel d), we see what appears to be a breakdown in the distinction between the stable and unstable regions, with the flow much less organized and filling most of the volume of the star. The narrow gap between the velocity contours and the surface of the star at late times arises from our sponging term. We look at the sensitivity of the results to the position of the sponge in the following subsection.

To get a better feel for the change in direction of the dipole, we compute the spherical angles, θ and ϕ, from $\langle \tilde{v}_r \rangle_i$, as defined above. Figure 7 shows these angles as a function of time. We see that both angles move through their full range many times over the course of the simulation. We see that the characteristic timescale for ϕ to complete a circuit through 2π is between 500 and 1000 s. At late times, it appears that the dipole is changing direction with a faster period, especially in the θ plot.

Figure 8 shows the peak radial velocity, $(v_r)_{\rm peak}$, inside the star, as a function of time. We see that it slowly rises with time, with a typical peak radial velocity of $\sim 10^7$ cm s^{-1}. Taking the convective region to have a radius of $R_{\rm conv} \sim 10^8$ cm, we define a lower bound to the convective turnover time of $2R_{\rm conv}/(v_r)_{\rm peak} = 20$ s.

Ignition will occur when the reactions proceed so strongly that hot, reacting bubbles are not quenched by adiabatic expansion in the convective motions carrying the fluid away from the center of the star. Since the $^{12}C + {}^{12}C$ reaction rate is so strongly temperature-sensitive, the peak temperature in the star serves as a good guide for observing the progression toward ignition. Figure 9 shows the peak temperature as a function of time for

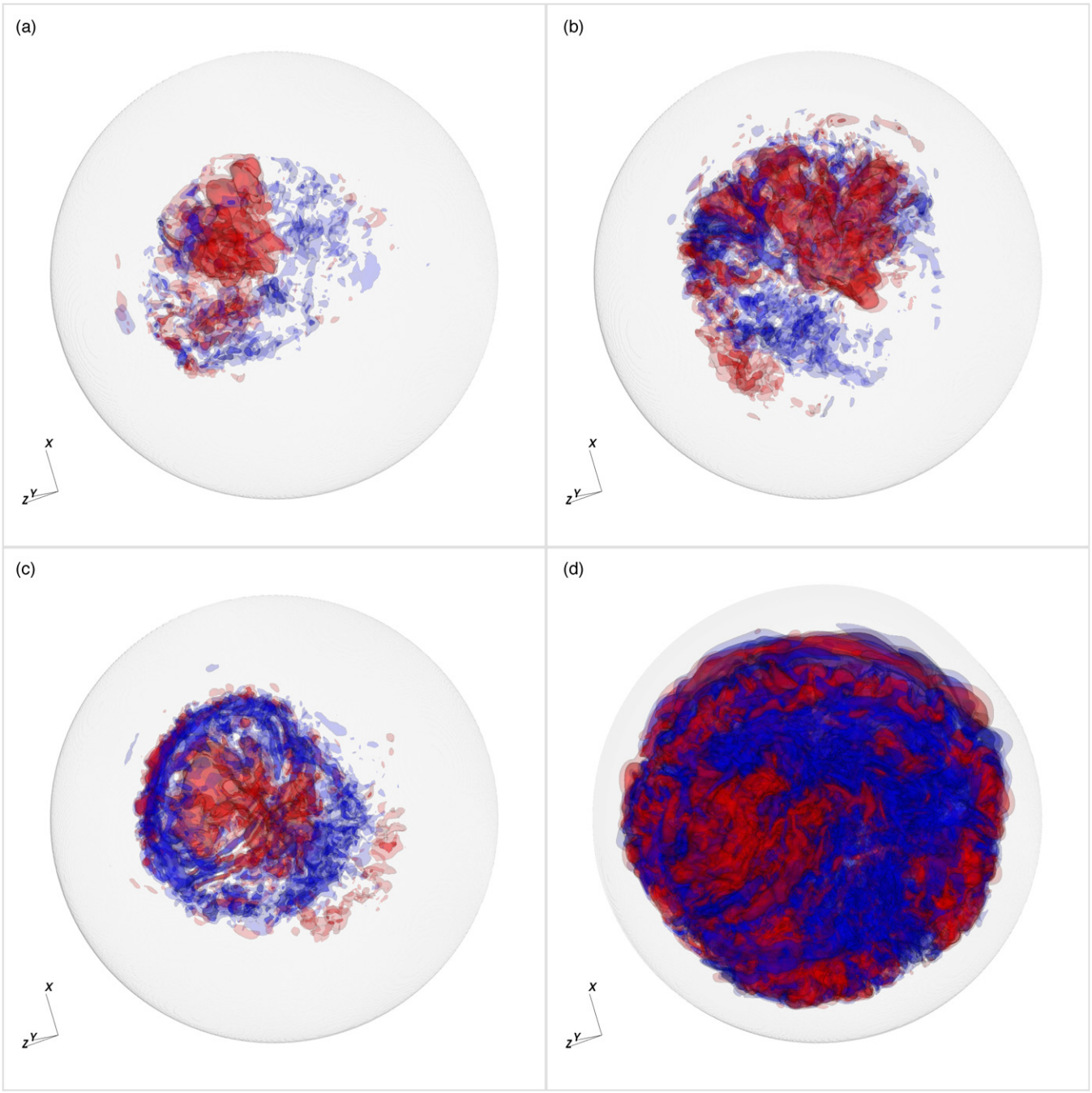

Figure 6. Radial velocity shown at 4 different times: (a) 800 s; (b) 3200 s; (c) 3420 s; (d) 7131.79 s. The latter time corresponds to the point of ignition. Red contours indicate outward moving fluid while blue contours indicate inward moving fluid. Two contour levels are used for each sign, $\pm 1.2 \times 10^6$ cm s^{-1} and $\pm 2 \times 10^6$ cm s^{-1}. The gray contour is a surface of constant density, $\rho = \rho_{\rm cutoff}$, marking the surface of the star.

this calculation. We see a short transient at the start of the calculation where the temperature quickly rises and then settles back down—this occurs from the nonlinear feedback of the temperature into the reactions when the flow field is not yet fully developed. After a short amount of time, a convective flow field develops that properly matches the energy generation at the center of the star, and the temperature settles into a long, gradual rise. About halfway through the calculation, we can clearly see that the temperature rise is nonlinear, and the temperature increase accelerates toward the very end, up to the point of ignition. The inset in Figure 9 shows the behavior of $T_{\rm peak}$ during the last 200 s.

The reactions dump energy into the star, and it heats up throughout. Figure 10 shows the average temperature at a given radius as a function of the radius at several different times. As we see, the temperature increases throughout the convective region. At late times, we see a distinct change in the temperature structure at the boundary of the convective region. This change in the temperature structure corresponds to the penetration of the vortical flow through the original boundary between the stable and unstably stratified regions in the vortical plot (Figure 5) shown above. It is not clear how robust this change in the character of the flow is to resolution—that is something that will be explored through higher resolution studies in the future.

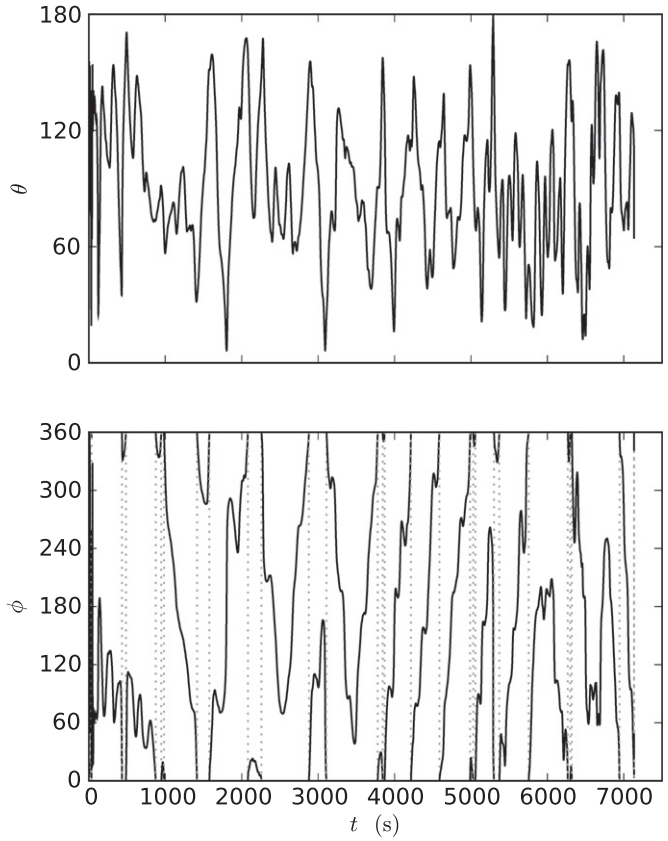

Figure 7. Spherical angles, θ and ϕ, computed from $\langle \tilde{v}_r \rangle_i$ as a function of time for the 384^3 calculation. The vertical dotted lines represent where the angle ϕ crosses the 0°–360° boundary, and are not really discontinuities. We see that the direction of the dipole changes constantly throughout the simulation.

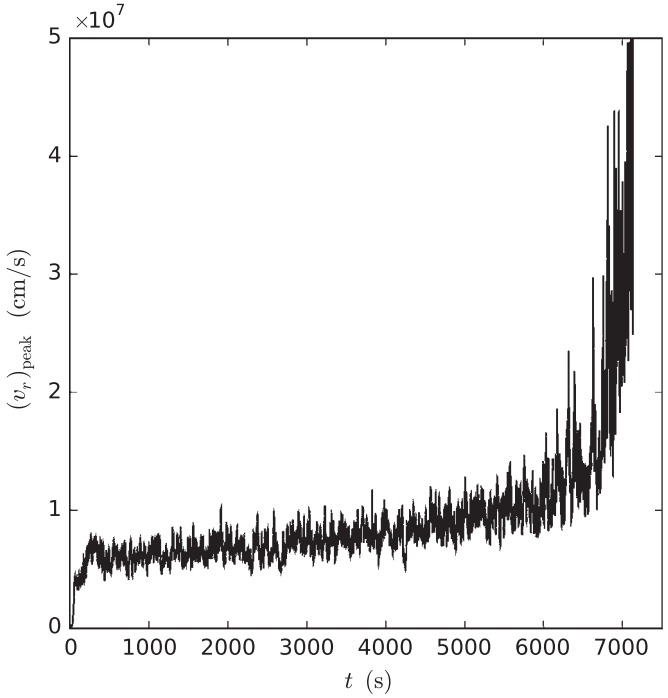

Figure 8. Peak radial velocity as a function of time for the 384^3 calculation.

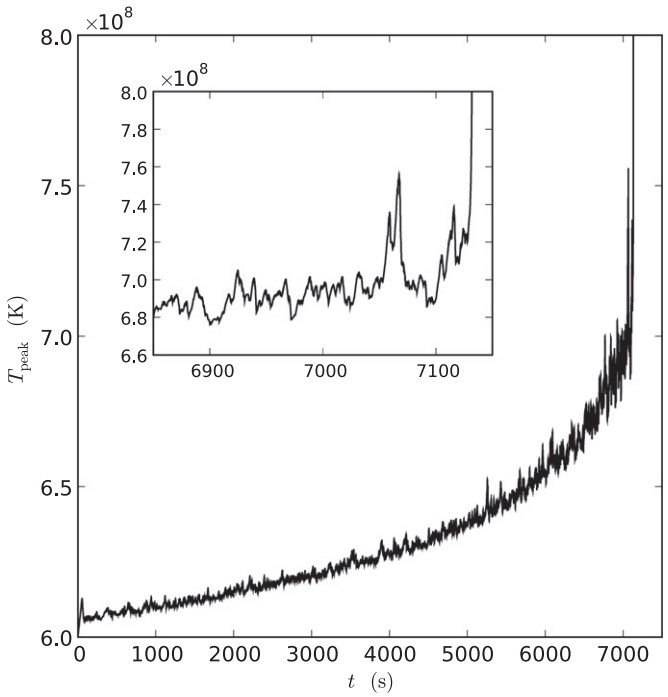

Figure 9. Maximum temperature in the white dwarf as a function of time for the 384^3 calculation. The temperature increase is highly nonlinear, ending at ignition. To show detail, we restrict the vertical range of the plot to 8×10^8 K. The inset shows the structure of $T_{\rm peak}$ during the last ∼200 s. We see large, but damped excursions in central temperature just prior to ignition.

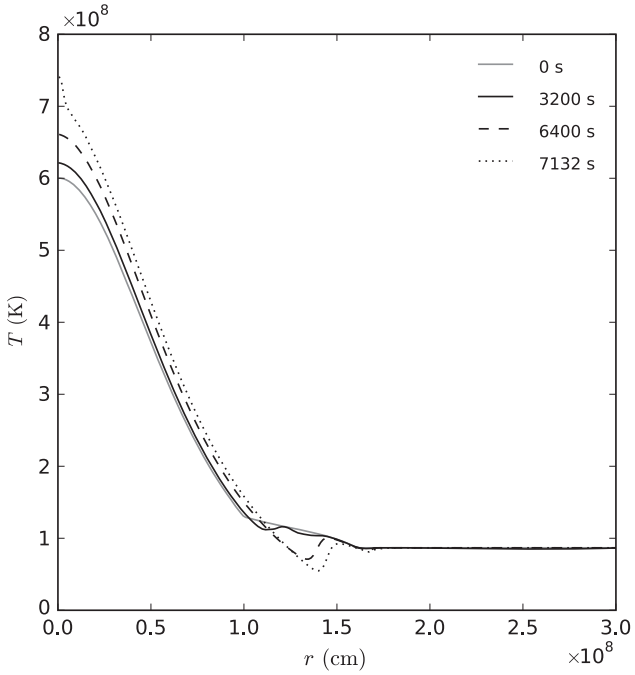

Figure 10. Average temperature as a function of radius in the white dwarf, shown at the initial time and three later times, for the 384^3 convection calculation. With time, the energy dumped into the star by reactions causes the temperature to increase throughout the star. The curve at 7132 s corresponds to the time of ignition.

It is also the case that those outer layers, near the transition to a stably stratified fluid, are where we would expect the expansion of the star to be greatest, so we need to check if neglecting the base state evolution was warranted. Figure 11 shows $(\delta\rho)_r/\langle\rho\rangle_r$ versus radius at several times. This is a measure of how much expansion of the star has taken place. If $(\delta\rho)_r$ is large compared to $\langle\rho\rangle_r$, then the full state is carrying the expansion rather than the base state, and as we have shown in Paper II, this can lead to

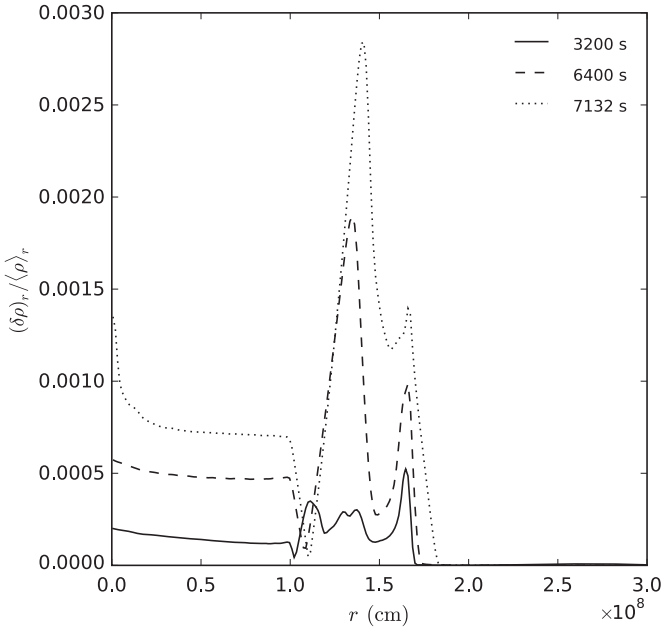

Figure 11. $(\delta\rho)_r/\langle\rho\rangle_r$ vs. r for the 384^3 white dwarf convection problem at three times. The curve at 7132 s corresponds to the time of ignition. We see that at all times, $(\delta\rho)_r/\langle\rho\rangle_r$ remains well below 1% everywhere inside the star.

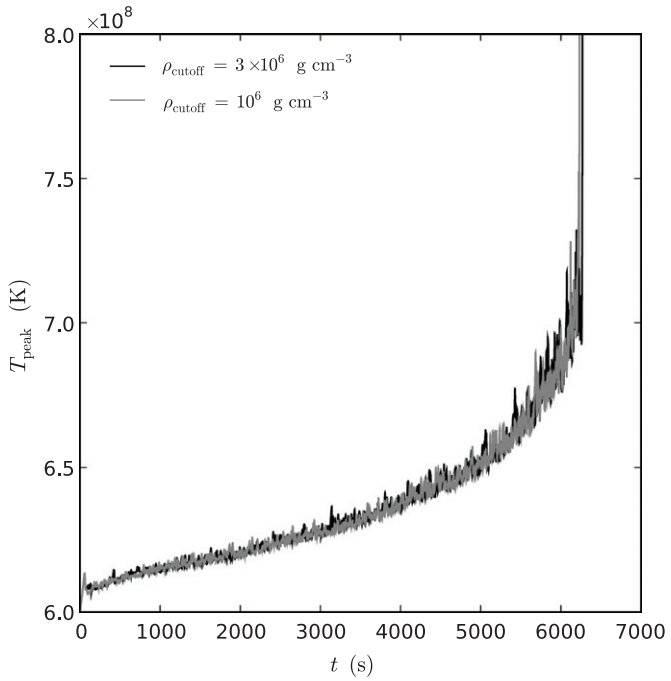

Figure 12. Maximum temperature in the white dwarf as a function of time for the two different choices of $\rho_{\rm cutoff}$ (10^6 g cm^{-3} and 3×10^6 g cm^{-3}). Both simulations use a 256^3 grid. Here we see excellent agreement between the two cases, indicating that the peak temperature is insensitive to our choice of $\rho_{\rm cutoff}$.

inaccuracies. As Figure 11 shows, $(\delta\rho)_r/\langle\rho\rangle_r$ is always below 1%, indicating that the departure from the base state is small, and any expansion would be minimal. In each case, the curve at 7132 s corresponds to the point is ignition, discussed below.

We can also look at the total kinetic energy in the star, which we compute as

$$K = \sum_{\Omega_{\rm star}} \rho |\mathbf{U}|^2 \Delta x \Delta y \Delta z. \quad (31)$$

At the point when the peak temperature reaches 8×10^8 K, the total kinetic energy inside the star is 6.24×10^{46} erg. To put this in context, we can compare the gravitational potential energy of the star, defined from our base state as

$$U = -\int_{\Omega_{\rm star}} \frac{GM(r)dM}{r}, \quad (32)$$

with $dM = 4\pi r^2 \rho_0 dr$. For our model, the gravitational potential energy is -3.2×10^{51} erg. The internal energy of the gas is also quite large, $E_{\rm int} = 2.7\times10^{51}$ erg, giving an energy difference of $\sim -5\times10^{50}$ erg that needs to be overcome to unbind the star. Therefore, kinetic energy release up to the point of ignition is a tiny fraction of what is needed to unbind the star, as expected.

The 384^3 calculation took 113,156 time steps to reach a simulation time of 7131.8 s—at which point the peak temperature had risen to 8×10^8 K, and ignition shortly followed. Overall, the average time step is 0.063 s. At this same instant, the Mach number, attained in the outer layers of the star, reached a value of 0.079. Earlier in the calculation, the maximum Mach number in the domain was considerably lower. For comparison, the highest sound speed in the star (at its center) is 9.5×10^8 cm s^{-1}, which would give a corresponding time step of 7×10^{-4} s (assuming a CFL number of 0.5, and $|U| \ll c_s$, where c_s is the sound speed).

3.2.3. Effect of $\rho_{\rm cutoff}$

As we noted above, the behavior of the coefficient in our constraint term and the location of the sponge are set by the density we refer to as $\rho_{\rm cutoff}$. To assess the influence of our choice of $\rho_{\rm cutoff}$, we perform a pair of simulations on a 256^3 grid that are identical except for the value of $\rho_{\rm cutoff}$. For our control case, we use $\rho_{\rm cutoff} = 3\times10^6$ g cm^{-3}, the value chosen for our main calculation. To explore the effects of lowering $\rho_{\rm cutoff}$, we also try a value of $\rho_{\rm cutoff} = 10^6$ g cm^{-3}. We note that the location of the sponge in the momentum equation remains keyed to the choice of $\rho_{\rm cutoff}$, so with the lower value of $\rho_{\rm cutoff}$, the location of the start of the sponge moves outward from the center of the star. In terms of mass, $\rho_{\rm cutoff} = 10^6$ g cm^{-3} means that the mass of the star enclosed is 1.381 $M_\odot$, compared to 1.378 $M_\odot$ with $\rho_{\rm cutoff} = 3\times10^6$ g cm^{-3}. The location of the start of the sponge contains 1.363 $M_\odot$, compared with 1.320 $M_\odot$ with $\rho_{\rm cutoff} = 3\times10^6$ g cm^{-3}.

Figure 12 shows $T_{\rm peak}$ as a function of time for the two calculations. As we see, the two curves track very well, indicating that the choice of $\rho_{\rm cutoff}$ has little influence on the temperature behavior near the center of the star. The time at which final ignition occurs differs between these two cases by only 38.4 s out of over 6000 s of evolution.

As noted above, the choice of $\rho_{\rm cutoff}$ is used to prevent the velocities from growing too large as the fluid experiences the steep density gradient at the edge of the star. We note that the time step the code takes with $\rho_{\rm cutoff} = 3\times10^6$ g cm^{-3} is 23% larger than with $\rho_{\rm cutoff} = 10^6$ g cm^{-3}. Thus, it is computational favorable to use the slightly higher value of the cutoff density.

3.2.4. Ignition

As the inset in Figure 9 shows, up to the point of ignition, the peak temperature rises rapidly, only to fall again, as a spark fails to ignite. Figure 13 shows the temperature structure in the last 500 s for the 384^3 calculation and both 256^3 calculations, shifted so the time of ignition lines up. All three runs show the peak temperature fluctuating rapidly before ignition, indicating some hot spots failed to ignite. In each case, eventually, a hot spot

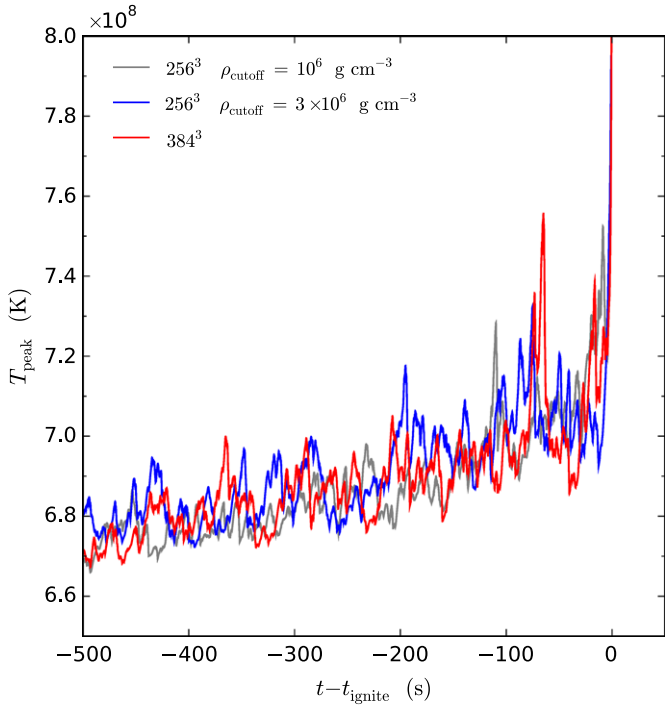

Figure 13. Peak temperature, $T_{\rm peak}$, as a function of time for the high resolution run (384^3) and two medium-resolution runs (256^3), offset so the time of ignition lines up. Here we show only the last 500 s leading up to ignition. We see that the temperature rise approaching ignition matches well between these different calculations.

burns faster than it cools and the temperature rapidly shoots up to over 10^{10}K—igniting the first flame. At this point, our algorithm cannot deal with the rapid energy release, and the low Mach number approximation breaks down, so we stop the calculation. Physically, at this point the nuclear burning timescale is much shorter than the advection timescale. Whether a second hot spot ignites shortly following this one is not something we can address presently.

At the point of ignition, the radial velocity (Figure 8) rises rapidly, reaching unphysically high values post-ignition—a symptom of the breakdown of the low Mach number method when the first flame ignites. However, prior to ignition, the algorithm remains valid, and we see that the radial velocities rise to $\sim$ few $\times 10^7$ cm s^{-1}. These velocities will affect the dynamics of the first flames to ignite.

To determine the location of the ignition, we compute the radius of the hot spot that ignited by looking at the peak temperature. We define the ignition radius as the position of the hot spot at the time when the peak temperature passes beyond 8×10^8 K. In all cases, once this temperature is exceeded, the temperature quickly shoots up to $O(10^{10})$ K.

For the high-resolution calculation, we find the location of ignition to be 21.6 km from the center of the star. The location of the peak temperature remained steady from (and possibly before) about 0.8 s before the peak temperature rose above 8×10^8 K, indicating that the hot spot was not moving very fast. The radial velocity in the zone with the peak temperature at the time we satisfy our ignition criteria is only 4.8 km s^{-1}. We note that physical center of the star is on a vertex on our Cartesian grid, so central ignition in this simulation would be at $\sqrt{3}\Delta x/2 = 11.3$ km, the distance from the center of the closest grid cell to the center of the star.

Figure 14 shows the perturbational temperature (full state temperature, T, minus the average temperature at the corresponding radius, $\langle T \rangle$) in the central 64^3 zones (833 km on a side). We have picked the location of the slice planes to cut right through the hot spot. As the figure shows, the peak temperature is strongly localized to a single zone, with an extended hot region surrounding this location.

For the two medium-resolution (256^3) cases, we find the location of the hot spot when $T_{\rm peak}$ crosses 8×10^8 K to be 84.5 km ($\rho_{\rm cutoff} = 3 \times 10^6$ g cm^{-3}) and 32.4 km ($\rho_{\rm cutoff} = 10^6$ g cm^{-3}). For reference, central ignition at this resolution would correspond to 16.9 km. For the $\rho_{\rm cutoff} = 3 \times 10^6$ g cm^{-3} case, the location of the peak temperature changes rapidly (moving outward from the center) as the peak temperature crosses 8×10^8 K, ranging from 32.4 km when $T_{\rm peak} = 7.51 \times 10^8$ K at 6267.6 s to 89.0 km when $T_{\rm peak} = 8.13 \times 10^8$ K at 6269.9 s. The radial velocity in the zone satisfying our ignition criteria is 39 km s^{-1}. Clearly, the flow dynamics at the location of ignition are significant in this case. We do not see movement of this magnitude for the $\rho_{\rm cutoff} = 10^6$ g cm^{-3} case, where the radial velocity in the zone satisfying our ignition criteria is only 2.9 km s^{-1}. For future calculations, we will store the location of the hot spot along with the peak temperature at every time step to help better understand these dynamics.

Taken together, we see a distribution of ignition radii in our results, ranging from 21.6 km to 89.0 km. Ignition is a highly nonlinear process, and we expect that were we to perform more runs, slightly tweaking the initial conditions, we would

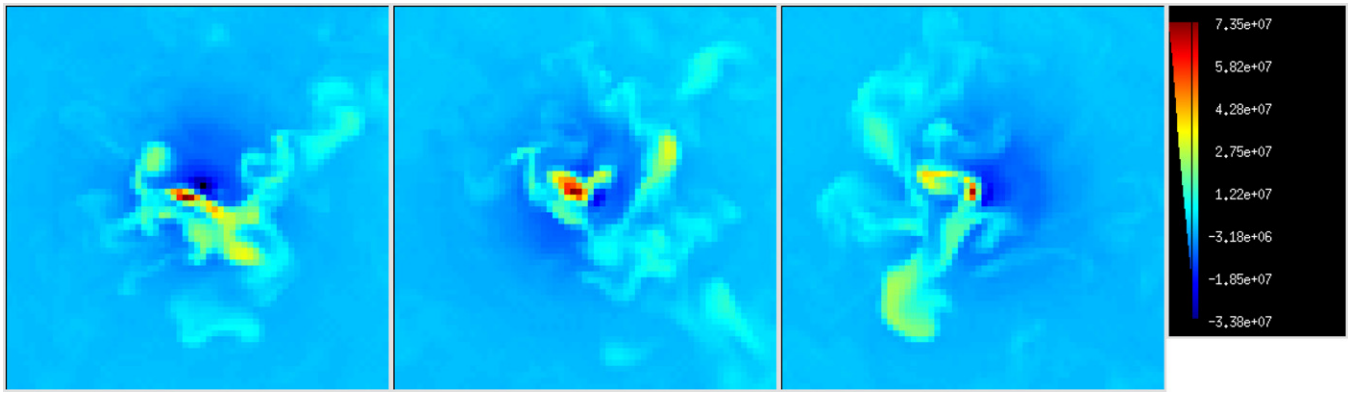

Figure 14. Perturbational temperature ($T - \langle T \rangle$) in three orthogonal slice planes (x–y, x–z, y–z) passing through the point (2.48×10^8 cm, 2.49×10^8 cm, and 2.52×10^8 cm), at a simulation time of 7131.79 s. Only the central 64^3 portion of the domain is shown (833.3 km on a side). Ignition occurs in the zone where $T - \langle T \rangle$ is the largest.

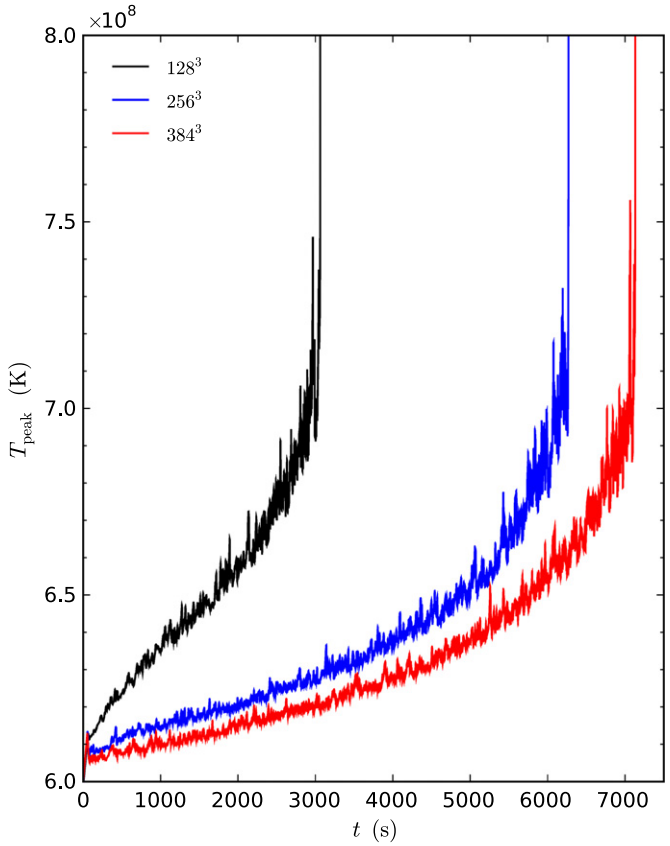

Figure 15. Peak temperature, $T_{\rm peak}$, in the white dwarf as a function of time for three different resolutions. We see that as we increase the resolution, the temperature increase is slower. The lowest resolution case reaches ignition very quickly. Once it ignites, the peak temperature climbs to $\sim 10^{10}$ K almost instantly. To show detail, we restrict the vertical range of the plot to 8×10^8 K.

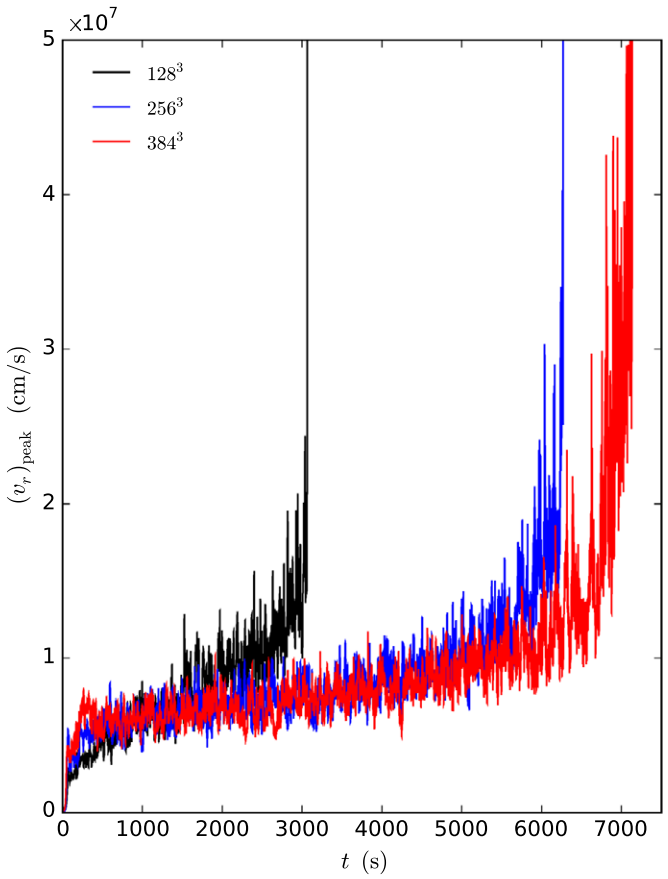

Figure 16. Peak radial velocity, $(v_r)_{\rm peak}$, in the white dwarf as a function of time for three different resolutions.

observe different values, all of which sample the distribution function of possible ignition locations in the problem. Owing to the stochastic nature of the problem, to really understand the ignition process requires performing a large number of slightly different calculations to map out the distribution function.

3.2.5. Effect of Resolution

It has been suggested that the behavior of convective flow can dramatically change in character at high Rayleigh number (Kadanoff 2001). In our simulation code, we do not explicitly add viscosity to the momentum equation (Equation (7)), so our Rayleigh number is determined by the numerical viscosity inherent in our advection scheme. Furthermore, the nature of the turbulence will depend on the Reynolds number of the flow, which again in our simulations is determined by numerical viscosity. Practically speaking, the way to increase the effective Reynolds and Rayleigh numbers of the simulation is to move to higher order advection methods and to increase the resolution.

While no amount of resolution will bring our effective Reynolds and Rayleigh numbers up to the $O(10^{14})$ and $O(10^{25})$ values, respectively, we expect in the true convecting white dwarf (Woosley et al. 2004), it is interesting to look at how the general results change with resolution. A second reason to explore resolution is that it is not known what size region will ignite. One might imagine that a region the size of only a few flame thicknesses needs to heat up to ignite a flame. At the central densities in the white dwarf, the flame thickness is $O(10^{-4}$ cm) (Timmes & Woosley 1992)—this is far below any resolution that can be obtained by a large-scale simulation code. However, the flame will initially burn in place, growing until it is large enough (about 1 km) that buoyancy becomes significant and it begins to rise and deform (Zingale & Dursi 2007). While this is still a smaller length scale than considered here, it is not out of reach with mesh refinement and larger computers.

To begin to understand the effect of resolution, we consider three cases: 128^3, 256^3, and 384^3, corresponding to physical zone sizes of 39.1, 19.5, and 13.0 km, respectively. We note that for the present study, computer resources prevent us from considering a 512^3 or higher case.

Figure 15 shows $T_{\rm peak}$ versus time for the three different resolutions. Immediately, we see that the 128^3 case reaches ignition much faster than the two higher resolution cases. In fact, from our starting temperature of 6×10^8 K, the highest resolution run takes more than twice as long in simulation time to reach ignition. Also apparent in the coarsest resolution run is that the temperature did not drop after the initial transient—this contributes to the faster overall evolution. Both of the higher resolution cases see a drop in the temperature after the initial transient, as the developing velocity field carries the heated fluid away from the center of the star. Close to ignition, the 256^3 and 384^3 runs show a similar slope in the $T_{\rm peak}$ versus t curve shown in Figure 13. The peak radial velocity as a function of time also shows differences between the resolutions, as shown in Figure 16. There does appear to be some convergence with resolution.

4. CONCLUSIONS AND DISCUSSION

We have demonstrated that our simulation code, MAESTRO, is capable of following the convective flow in a white dwarf leading up to the ignition of a Type Ia supernova. We have explored the sensitivity of the results to resolution and to the choice of low-density cutoff, $\rho_{\rm cutoff}$. Our test problem shows that discretizing the star on a Cartesian grid with a radial base state leads to an accurate representation of the flow.

Over many convective turnover times, our simulations capture the rise of the peak temperature in the white dwarf up to ignition, recover the dipole nature of the convective flow first shown in Kuhlen et al. (2006), and track the change in direction of the dipole. We see, for the first time in multidimensional simulations, the distinct change in the nature of the flow at the outer boundary of the convective region, as discussed in Piro & Chang (2008). The late time breakdown of this interface needs further investigation.

All of our models reached ignition. For the two medium-resolution runs, the ignition occurred at a radius of 32.4 and 84.5 km. For the high-resolution run, it occurred at 21.6 km. These are the locations of the first flames. We note that this is a highly nonlinear problem, and small changes in the state of the star could affect the ignition process. To really understand the statistical distribution of initial ignition points requires running a suite of calculations, varying the initial model (central density, size of initial convective region), and the initial state of the star. With an ensemble of such calculations, we could get a much better understanding of the ignition process. We also need to understand how the ignition process differs with higher resolution.

A detailed comparison to Höflich & Stein (2002) or Kuhlen et al. (2006) is difficult, because of the differing geometries used. Höflich & Stein (2002, henceforth HS) simulated a 90° wedge in two dimensions, but cut out the innermost 13.7 km (in their "extended computational domain" run). As we discussed in the present calculation, the burning is strongly peaked near the center of the star, so cutting out the center would miss a great deal of the energy generation. It would also prevent the fluid from flowing through the center of the star, which is the dominant pattern seen in the present calculation. Because HS used a spherical grid, and allowed the radial spacing to vary, there is no single grid resolution for their simulation, but they state that near the inner boundary, the grid resolution is "$\sim$ 2 km"—about 6× finer than the uniform resolution we use throughout the star. In both their and our calculations, several hours of the runaway are followed leading up to the point of ignition ($\sim$ 3 hr for HS, $\sim$ 2 hr for our calculation). Also, in both cases, the ignition takes place in a single zone. However, the details of the ignition differ, because HS have an inner boundary and a wedge-shaped domain compression is generated that leads to the ultimate ignition near the center. In our calculation, we have flow through the center throughout the simulation. HS found the ignition to take place at a radius of 27 km in their model, which is within the range we report in our study. Furthermore, because their initial model had a strong gradient in the carbon mass fraction, with the outer portion of the star having a carbon mass fraction of 0.4 and the core having a value close to 0.25 (see HS, Figure 1), HS report that the expanding convective region results in an increase in the carbon mass fraction at the center from 0.25 to 0.36. This is not the case in our model, where the carbon burning caused a 0.5% decrease in the central carbon mass fraction over the time we modeled. HS quote convective velocities between 40 and 120 km s^{-1} at ignition. In our case, the radial velocities were around 100 km s^{-1} for most of the evolution, rising to several times that just before ignition.

The calculation by Kuhlen et al. (2006, henceforth KWG) modeled the star in three dimensions, with an inner boundary at 50 km, again cutting out the center of the star. They also put the outer boundary at 500 km, which is approximately halfway through the convectively unstable region in the initial model (KWG and the present study use very similar initial models, generated from the Kepler stellar evolution code). Despite cutting out the center, KWG found that a large-scale dipole flow pattern dominates—similar to what we see (although we note that they also did a rotating model, and saw the dipole break down). Unlike HS or the present calculation, KWG do not model the evolution continuously leading up to ignition, but rather model two snapshots in time, corresponding to central white dwarf temperatures of 7×10^8 K and 7.5×10^8 K, with durations of 70 and 41 s, respectively. This amounts to a few turnover times (Kuhlen et al. 2006). It is difficult to compare resolution with KWG, as they use a spectral method for the spatial discretization. KWG quote typical velocities of 50–100 km s^{-1}—consistent with both HS and the present calculation. Finally, in contrast to both HS and our calculation, KWG did not follow the evolution to the ignition of the first flame, but rather inferred from the size of the dipole flow pattern that ignition would likely be off-center. Overall the comparison to these previous calculations, and the variation seen in our own set of calculations, suggest that more full-star, three-dimensional calculations, with varying initial parameters, are needed to fully understand the ignition process.

Future work will include both algorithmic improvements and more realistic physics. The focus of the next set of calculations will be to continue exploring the nature of the convection. On the algorithmic front, we will switch to an unsplit implementation of the piecewise parabolic method (Colella & Woodward 1984; Miller & Colella 2002) for the advection scheme and begin to incorporate adaptive mesh refinement. Together with an increase in grid resolution, these changes will allow us to push to higher effective Reynolds numbers. Physically, we will improve the nuclear energetics, add an enthalpy equation to better define the temperature throughout the simulation, incorporate the expansion of the base state, and include rotation. Numerical (Kuhlen et al. 2006) and analytic (Piro 2008) works have shown that the effects of rotation can be significant.

The present calculations show only the ignition of the first flame, but the convection continues, and it is likely that other flames will ignite. This process of ongoing ignition could be critical to the understanding of SNe Ia. To date, only limited studies (Schmidt & Niemeyer 2006) have been performed investigating the effects of temporally spaced ignition spots. By capturing the flames that ignite in our simulations and propagating them in a controlled fashion, we can continue a convective calculation to simulate the formation of additional ignition spots.

Presently, our algorithm is unable to follow the evolution past the point where ignition occurs. However, right up until that point, the model remains valid. Therefore, these models can still provide useful starting conditions for explosion models run with fully compressible codes, simply by mapping the fully convective state right before ignition into a three-dimensional compressible code. On the longer term, an extension of our method to include long wavelength acoustics would extend the validity of this method to $M \sim 1$ (see, for example, Gatti-Bono

& Colella 2006). We will also work on incorporating a flame model to capture the ignition of the flame(s) on the grid, so that we may continue the convective calculation in the presence of these first flames.

We thank Frank Timmes for making his equation of state routines publicly available. We thank Alan Calder, Jonathan Dursi, and Chris Malone for many useful discussions on this work. Finally, we thank Mike Lijewski for his continued help on software development. The work at Stony Brook was supported by a DOE/Office of Nuclear Physics Outstanding Junior Investigator award, grant no. DE-FG02-06ER41448, to Stony Brook. The work at LBNL was supported by the SciDAC Program of the DOE Office of Mathematics, Information, and Computational Sciences under the U.S. Department of Energy under contract no. DE-AC02-05CH11231. The work at UCSC was supported by the DOE SciDAC program under grant no. DE-FC02-06ER41438.

Computer time for the main calculation in this paper was provided through a DOE INCITE award at the Oak Ridge Leadership Computational Facility (OLCF) at Oak Ridge National Laboratory, which is supported by the Office of Science of the U.S. Department of Energy under contract no. DE-AC05-00OR22725. We thank Bronson Messer for his help with this machine. Computer time for the supporting calculations presented here was provided by Livermore Computing's Atlas machine through LLNL's Multiprogrammatic & Institutional Computing Program. The test problem calculation used resources of the Argonne Leadership Computing Facility at Argonne National Laboratory, which is supported by the Office of Science of the U.S. Department of Energy under contract DE-AC02-06CH11357. Some visualizations were performed using the VisIt package. We thank Gunther Weber for his assistance with VisIt.

REFERENCES

Alastuey, A., & Jancovici, B. 1978, ApJ, 226, 1034
Almgren, A. S., Bell, J. B., Nonaka, A., & Zingale, M. 2008, ApJ, 684, 449 (Paper III)
Almgren, A. S., Bell, J. B., Rendleman, C. A., & Zingale, M. 2006a, ApJ, 637, 922 (Paper I)
Almgren, A. S., Bell, J. B., Rendleman, C. A., & Zingale, M. 2006b, ApJ, 649, 927 (Paper II)
Bychkov, V. V., & Liberman, M. A. 1995, A&A, 304, 440
Colella, P. 1990, J. Comput. Phys., 87, 171
Colella, P., & Woodward, P. R. 1984, J. Comput. Phys., 54, 174
Fryxell, B., et al. 2000, ApJS, 131, 273
Gamezo, V. N., Khokhlov, A. M., & Oran, E. S. 2005, ApJ, 623, 337
García-Senz, D., & Bravo, E. 2005, A&A, 430, 585
Garcia-Senz, D., & Woosley, S. E. 1995, ApJ, 454, 895
Gatti-Bono, C., & Colella, P. 2006, J. Comput. Phys., 216, 589
Graboske, H. C., Dewitt, H. E., Grossman, A. S., & Cooper, M. S. 1973, ApJ, 181, 457
Höflich, P., & Stein, J. 2002, ApJ, 568, 779
Hillebrandt, W., & Niemeyer, J. C. 2000, ARA&A, 38, 191
Iapichino, L., Brüggen, M., Hillebrandt, W., & Niemeyer, J. C. 2006, A&A, 450, 655
Itoh, N., Totsuji, H., Ichimaru, S., & Dewitt, H. E. 1979, ApJ, 234, 1079
Jordan, IV, G. C., Fisher, R. T., Townsley, D. M., Calder, A. C., Graziani, C., Asida, S., Lamb, D. Q., & Truran, J. W. 2008, ApJ, 681, 1448
Kadanoff, L. P. 2001, Phys. Today, 54, 34
Kuhlen, M., Woosley, S. E., & Glatzmaier, G. A. 2006, ApJ, 640, 407
Livne, E., Asida, S. M., & Höflich, P. 2005, ApJ, 632, 443
Miller, G. H., & Colella, P. 2002, J. Comput. Phys., 183, 26
Niemeyer, J. C., Hillebrandt, W., & Woosley, S. E. 1996, ApJ, 471, 903
Nomoto, K., Thielemann, F.-K., & Yokoi, K. 1984, ApJ, 286, 644
Piro, A. L. 2008, ApJ, 679, 616
Piro, A. L., & Chang, P. 2008, ApJ, 678, 1158
Röpke, F. K., Hillebrandt, W., Schmidt, W., Niemeyer, J. C., Blinnikov, S. I., & Mazzali, P. A. 2007, ApJ, 668, 1132
Saltzman, J. 1994, J. Comput. Phys., 115, 153
Schmidt, W., & Niemeyer, J. C. 2006, A&A, 446, 627
Stein, J., & Wheeler, J. C. 2006, ApJ, 643, 1190
Timmes, F. X. 2008, Stellar Equations of State (Tempe, AZ: Arizona St. Univ, SESE), http://cococubed.asu.edu/code_pages/eos.shtml
Timmes, F. X., & Swesty, F. D. 2000, ApJS, 126, 501
Timmes, F. X., & Woosley, S. E. 1992, ApJ, 396, 649
Weaver, T. A., Zimmerman, G. B., & Woosley, S. E. 1978, ApJ, 225, 1021
Woosley, S. E. 1990, in Supernova, ed. A. G. Petschek (New York: Springer), 182
Woosley, S. E., Wunsch, S., & Kuhlen, M. 2004, ApJ, 607, 921
Woosley, S. E., et al. 2007, J. Phys. Conf. Ser., 78, 012081
Wunsch, S., & Woosley, S. E. 2004, ApJ, 616, 1102
Yoon, S.-C., Podsiadlowski, P., & Rosswog, S. 2007, MNRAS, 380, 933
Zingale, M., & Dursi, L. J. 2007, ApJ, 656, 333
Zingale, M., et al. 2002, ApJS, 143, 539